ACS APPLIED MATERIALS & INTERFACES

Research Article

www.acsami.org

Cellulose-Templated Graphene Monoliths with Anisotropic Mechanical, Thermal, and Electrical Properties

Rujing Zhang,[†] Qiao Chen,[†,‡] Zhen Zhen,[†,‡] Xin Jiang,[†,‡] Minlin Zhong,[†] and Hongwei Zhu*[,†,‡]

[†]School of Materials Science and Engineering, State Key Laboratory of New Ceramics and Fine Processing and [‡]Center for Nano and Micro Mechanics, Tsinghua University, Beijing 100084, China

Supporting Information

ABSTRACT: Assembling particular building blocks into composites with diverse targeted structures has attracted considerable interest for understanding its new properties and expanding the potential applications. Anisotropic organization is considered as a frequently used targeted architecture and possesses many peculiar properties because of its unusual shapes. Here, we show that anisotropic graphene monoliths (AGMs), three-dimensional architectures of well-aligned graphene sheets obtained by a dip-coating method using cellulose acetate fibers as templates show thermal-insulating, fire-retardant, and anisotropic properties. They exhibit a feature of higher mechanical strength and thermal/electrical conductivities in the axial direction than in the radial direction. Elastic polymer resins are then introduced into the pores of the AGMs to form conductive and flexible composites. The composites, as AGMs, retain the unique anisotropic properties, revealing opposite resistance change under compressions in different directions. The outstanding anisotropic properties of AGMs make them possible to be applied in the fields of thermal insulation, integrated circuits, and electromechanical devices.

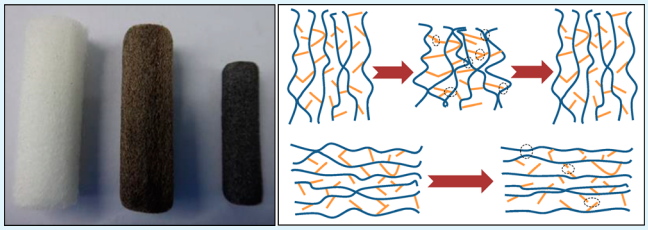

KEYWORDS: *graphene, anisotropic, monolith, multifunctional, composite*

1. INTRODUCTION

Assembling particular building blocks into composites with diverse targeted structures has attracted considerable interests for understanding its new properties and expanding the potential applications. In nature, there are many materials with subtle microstructures. For example, wood, as a fiber-matrix composite with cellular microstructure, has remarkably high strength and stiffness and low density[1,2] with apparent anisotropic properties at both longitudinal and latitudinal directions. Anisotropic organization is considered as a frequently used targeted architecture and possesses many peculiar properties because of its unusual shapes.[3−5] A variety of building blocks, such as nanoparticles,[3,4] nanosheets,[5] and nanotubes,[6] were assembled along aligned orientation to prepare materials with anisotropic structures. For example, the anisotropic architectures of carbon materials, such as carbon nanotubes[7,8] and carbon black particles,[9] have been widely researched, demonstrating that they have high electrical and thermal conductivity, as well as excellent mechanical properties, along the aligned direction of the building blocks.

Graphene, as one of the promising carbon materials, has been widely investigated since its discovery. Study on the synthesis of graphene-based macroscopic materials from one-dimensional (1D) to three-dimensional (3D) is one of the fastest growing fields in the past several years because of the excellent mechanical strength and electrical conductivity. For example, the graphene sheets of 1D graphene fibers, prepared by wet-spinning method[10] and dimensionally confined hydrothermal strategy,[11] were highly oriented and closely packed. The fibers showed the features of high fracture strength (500 MPa) and electrical conductivity (4.0×10^4 S/m) in the longitudinal direction.[12] Two-dimensional (2D) graphene-based papers obtained by vacuum filtration method consisted of graphene sheets with layered structures[13−17] and had excellent electrical properties. However, few studies have been focused on 3D graphene sheets with well-aligned architecture. The typical methods to prepare porous 3D-structured graphene with high symmetry include reduction self-assembly approach.[18−23] and cross-linking strategy.[24−26] The nondirectional gelation of graphene oxide (GO) sheets takes place in the suspension through supermolecular interactions. The template-directed method is usually used in preparation of anisotropic structured materials among the various approaches. However, the templates in previous studies, such as nickel foam,[27] PU sponge,[28,29] particles,[30,31] and bubbles,[32] did not exhibit obvious anisotropy. Similar to the anisotropic growth of ice crystals based on the rejection and separation effect,[33] graphene-based materials with sheets orienting along the freezing direction were prepared by freeze-casting methods.[34,35] An unique cellular-structured natural cork has been fabricated with graphene sheets well-oriented in a nearly parallel manner,[36] showing superelasticity and reinforcement in hydro-

Received: June 1, 2015
Accepted: August 18, 2015
Published: August 18, 2015

DOI: 10.1021/acsami.5b04808
ACS Appl. Mater. Interfaces 2015, 7, 19145−19152

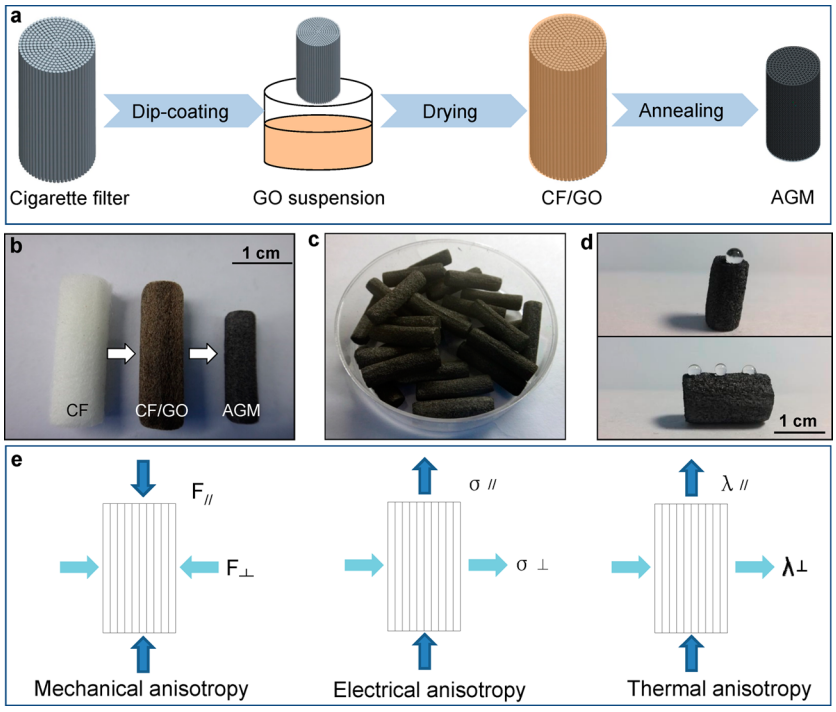

Figure 1. (a) Schematic illustration of the fabrication process of AGM. Photographs of (b) CF template, CF/GO, and AGM and (c) AGMs. (d) Photograph showing water drops stayed on the surface showing the hydrophobicity of AGM. (e) Schematic diagrams of the main research content, including anisotropic mechanical, electrical, and thermal properties of AGMs.

gels.[37] However, as compared in Supplementary Table S1, the concept of anisotropic graphene monolith has rarely been proposed, and anisotropic properties of the materials have not been well-explored.

In this work, an anisotropic graphene-based monolith (AGM) with cellulose acetate fibers (derived from cigarette filters, CFs) as templates was prepared and characterized. The structure of the obtained graphene monoliths revealed that distorted graphene microtubes, to a certain extent, were aligned with graphene sheets as connections. The materials possessed obviously higher electrical and thermal conductivities in the axial direction, nearly parallel to the microtubes, than in the radial direction, nearly normal to the microtubes. Nanocomposites with the continuous conductive network of AGM in elastic polymer of polydimethylsiloxane (PDMS) were further successfully synthesized. AGM served as an effective reinforcement of the polymer, increasing its electrical conductivity and mechanical strength. The unique resistance change of AGM/PDMS composites under compression would provide potential applications in electromechanical sensors.

2. EXPERIMENTAL SECTION

Materials. GO powder was purchased from XFNANO Materials Tech Co., Ltd. Cigarette filters were collected from HONGMEI made by HONGTA TOBACCO (GROUP) Co., Ltd. PDMS base agent and curing agent were purchased from Dow Corning. The high purity silver paint was purchased from SPI.

Synthesis of AGMs. GO was dispersed in water by ultrasonication for 2 h to prepare a GO suspension (5 mg mL^{-1}). The paper covers wrapped on the cigarette filters were removed, and then the filters were immersed into the GO suspension for 30 min until the GO adsorption was saturated. The resulting CF/GO composite was then dried in the oven at 80 °C. This dip-coating plus drying process was repeated for three times. AGMs were finally obtained by annealing CF/GO solids in a thermal furnace at 1000 °C for 1 h in Ar.

Fabrication of AGM/PDMS Composites. PDMS base agent was mixed with curing agent with a weight ratio of 10:1 to prepare a homogeneous solution. AGMs were then immersed into the PDMS solution. After 2 h vacuum filtration, AGMs were taken out from the solution and cured in a vacuum oven at 50 °C for 12 h to obtain AGM/PDMS composites.

Characterization of Morphology and Elements. Scanning electron microscopy (SEM) images of the materials were obtained with a field-emission electron microscope (FEI QUANTA 450 FEG). Thermal gravity analysis (TGA) was measured with a NETZSCH STA 449F3 instrument. X-ray diffraction (XRD) patterns of the materials were performed with a Bruker AXS D8 ADVANCE X-ray diffractometer. X-ray photoelectron spectroscopy (XPS) was carried out with an ESCALAB 250Xi system. Raman spectra were recorded with a HORIBA LabRAM HR high-resolution Raman microscope system. The surface area was measured using Brunauer–Emmett–Teller (BET) method with an Aurosorb-iQ2-MP analyzer through nitrogen adsorption.

Measurements of Mechanical, Thermal, and Electrical Properties. The compression properties were evaluated with a testing instrument INSTRON 5943. The electrical and thermal conductivities of AGM and AGM/PDMS composites were carried out at 300 K on a comprehensive physical property testing system (QUANTUN PPMS-9). Properties in both the axial and radial directions were measured.

Testing of Electromechanical Properties and Resistance–Temperature Relationship of AGM/PDMS Composite. Silver wires were connected to the two ends of the materials as electrodes by silver paste. For the measurement of electromechanical properties, the materials were compressed with the previously mentioned INSTRON 5943. At the same time, the resistance was recorded with a Keithley 4200. Different strains (10%, 30%, and 50%), cycles, and frequencies were conducted both in the radial and axial directions. For the testing of the resistance–temperature relationship, the prepared composites with silver wire electrodes were first put in an oven with a specific temperature. The materials were kept for about 10 min at the preset temperature until the temperature uniformly distributed in the composites. Then the resistance was measured with a Keithley 4200.

DOI: 10.1021/acsami.5b04808
ACS Appl. Mater. Interfaces 2015, 7, 19145–19152

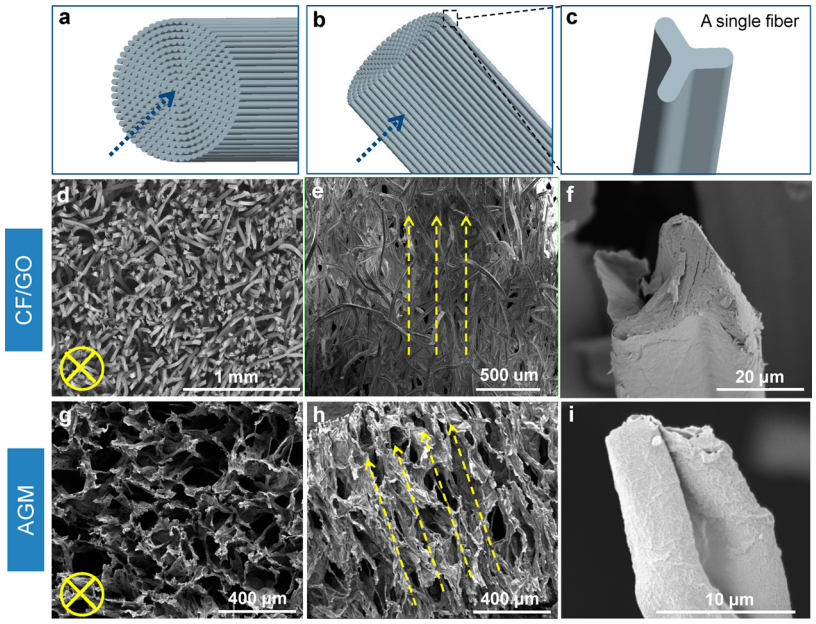

Figure 2. (a–c) Schematic illustrations of the monoliths observed at different angles of view. (d–f) SEM images of the CF/GO monoliths, with gold coating on the surface. (g–i) SEM images of AGMs. (d, g) Cross-sectional view. (e, h) Lateral view. The symbols in d and g reflect directions parallel to the axes, together with the arrows in e and h, indicating the axial direction of the fibers.

The tested temperature ranged from 30 to 180 °C for three cycles. Resistances in both the axial and radial direction were measured.

3. RESULTS AND DISCUSSION

AGMs were prepared by a dip-coating method with subsequent drying and annealing as the procedure in Figure 1a. The templates of CFs were first put into an aqueous solution of GO with a concentration of 5 mg mL^{-1} until the solution was fully absorbed. The GO sheets were then coated on the backbone in a subsequent drying process. Both dip-coating and drying processes were repeated three times to obtain a sufficient thickness of GO layer. The AGMs were finally obtained by annealing CF/GO at 1000 °C for 1 h, in which the templates were thermally decomposed and GO sheets were reduced synchronously. After being coated by GO sheets, the color of CF templates was turned from white to brown with an unconspicuous volume change, as shown in Figure 1b. The volume of CF/GO was obviously changed after the annealing process, while the cylinder shape was retained (Figure 1c). The dramatic change resulted from the transformation of CF into brittle hierarchical porous carbon structures,[38] as shown in Supplementary Figure S1a. The TGA result indicated that the carbon yield of CF in the carbonization process was about 10%, in good agreement with previous research,[39] as shown in Supplementary Figure S1b.

Because of the significant change of CF in both the shape and the mass in the annealing process, the layer of GO coated on the backbone should be thick enough to keep the initial shape of the templates. That is why the dip-coating and drying process need to be repeated three times. Figure S1c shows AGMs obtained through repeating the treatment once (left), twice (middle), and three times (right) with GO concentration of 5 mg mL^{-1}. Distorted monoliths were observed when samples were treated once or twice. However, if the GO concentration was as low as 2 mg·mL^{-1}, the cylinder shape could not be maintained even after repeating the treatment three times. AGM exhibited good hydrophobicity in both the axial and radial directions, as shown in Figure 1d. Here we mainly discuss the mechanical, electrical, and thermal properties along and vertical to the axis of AGMs. Schematic diagrams in Figure 1e show the tested parameters and directions. The experimental results obtained in this work revealed obviously anisotropic structure and properties.

The morphologies of CF/GO and AGM were demonstrated by SEM. Parts a–c of Figure 2 show the directions of the observation. Aligned fibers were observed for initial CF templates composed of cellulose acetate, as displayed in Supplementary Figure S2a–c. The fiber surface was smooth with a "Y"-shape cross-section, as shown in Supplementary Figure S2c. It indicated that a continuous and uniform GO layer was formed on the surface of cellulose acetate fiber after dip-coating and drying processes. The images of the top view and section view of CF/GO were shown in Figure 2d,e, respectively. The fibers were relatively ordered. The slight bending and cross-linking of the fibers would enhance the integral strength of the composite through preventing fibers from scattering under pressure. The fibers were connected together to form a piece by GO sheets (Figure 2e). The cross-section of the fibers in CF/GO retained the Y-like shape, as shown in Figure 2f, with a thick GO layer on the surface. After annealing at 1000 °C, ordered graphene microtubes connected by graphene sheets were obtained. The obtained AGM exhibited apparent anisotropic structure perpendicular and parallel to the axial direction, as shown in Figure 2g,h. Honeycomb-like structures with pores in a range of 100–300 μm were observed in the cross-section images along the axis (Figure 2g). Due to the dramatic pyrolysis of the templates, single fibers of CF/GO were transformed into distorted and shrunken microtubes (Figure 2i). The diameter of the microtubes was in several micrometers.

XRD patterns of the materials were shown in Supplementary Figure S3. It was found that CFs were composed of cellulose acetate. The peaks of anatase TiO_2,[38] which is used as a typical photocatalyst to prepare CFs,[40] were observed in CFs. After

DOI: 10.1021/acsami.5b04808
ACS Appl. Mater. Interfaces 2015, 7, 19145–19152

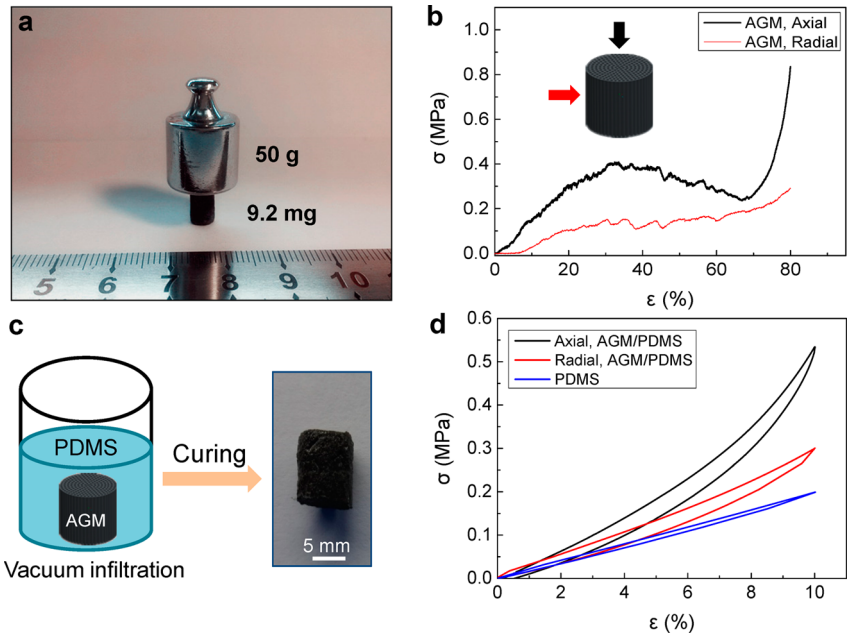

Figure 3. Mechanical anisotropy of AGM. (a) Photograph showing an AGM monolith of 9.2 mg can sustain a 50 g weight. (b) Compressive stress−strain measurements of AGM in axial and radial directions. (c) Schematic illustration of the AGM/PDMS composite fabrication. (d) Compressive stress−strain curves of the AGM/PDMS composite and pure PDMS.

being pyrolyzed at 1000 °C for 1 h, the CF templates were transformed to nongraphitic carbons, with obvious diffraction peaks at 2θ of 24°, 44°, and 83°.[39] The peak at 2θ of ∼10.5° corresponded to an interlayer spacing of 0.83 nm, suggesting the existence GO. The broad diffraction peak of AGM indicated the formation of graphitic microcrystals during the thermal reduction process of GO.[21] The reduction of GO during the annealing process was testified by XPS. The significant reduction of oxygen-containing functional groups, including C−O, C═O, and O−C═O, was observed at 286.4, 288.0, and 289.6 eV, respectively (Figure S4a,b). Raman spectra are shown in Figure S4c. The bands of D and G and 2D bands were observed, and the decrease of the intense ratio (I_G/I_D) reveals reduction of GO, as reported by many other researchers in previous reports.[26] The D band at 1355 cm^{-1} was attributed to defects of the sample. The Brunauer−Emmett−Teller (BET) specific surface area of AGM was calculated as 126 $m^2 \cdot g^{-1}$ from the nitrogen adsorption isotherm, as shown in Figure S4d. On comparison with previous reports,[41−43] the BET specific surface area of AGM in this work was within the normal range.

An AGM monolith of 9.2 mg could bear a weight of 50 g along the axial direction, as shown in Figure 3a. It was about 5500 times its own weight. Three regions can be seen in the stress−strain curves of AGM monolith in Figure 3b. The initial growth region was attributed to the cell edge bending and the local distortion. The stress reduction region was attributed to the extensive brittle collapse. The significant stress increase region was attributed to the densification of the collapsed material.[2,44] It revealed that the AGM had a typical feature of anisotropic cellular foam of significantly higher strength in the axial direction than in the radial direction.[45] This is due to the template-induced alignment of graphene sheets along the axis.

Introducing a continuous network of carbon nanomaterials into polymer hydrogels is often used to enhance the mechanical strength of materials.[37] PDMS was introduced into the pores of AGMs through a vacuum infiltration method. AGM/PDMS composites can be obtained with a subsequent curing process, as shown in Figure 3c. Based on the compressive stress−strain curve in Figure 3d, the mechanical strength of PDMS in the axial direction seemed to be more enhanced than that in the radial direction, in accordance with the mechanical anisotropic property of AGM. Compared with the pure PDMS, the Young's modulus of the AGM/PDMS composite is increased by a factor of 1.46 and 2.5 in the axial and radial directions, respectively (Table S2). Compared with some previously reported reinforcements for PDMS, AGM shows unique anisotropic enhancement. (Table S3)

Parts a−c of Figure 4 show the fire resistance of AGM. A burning experiment was carried out on an alcohol lamp for the CF template, CF/GO, and AGM. The CF template was easily ignited and melted simultaneously, resulting in brittle black materials, as shown in the lower inset in Figure 4a. The CF/GO cannot resist flame either even though being coated by GO, resulting in a shrunken monolith. The AGM exhibited a good thermal stability against burning, as shown in Figure 4c. Its initial cylinder shape was not changed in the burning process due to the removal of the flammable template. Because graphene microtubes were mostly ordered, the thermal conductivity of AGM in the axial direction ($\lambda_{//}$ = 74.3 $mW \cdot K^{-1} \cdot m^{-1}$) was apparently higher than that in the radial direction ($\lambda_{\perp}$ = 29.9 $mW \cdot K^{-1} \cdot m^{-1}$), as a consequence of fast thermal radiation, conduction, and convection.[45] As a continuous thermal and electrical conductive network, AGM can serve as fillers in polymers to form reinforced graphene-based nanocomposites. The AGM/PDMS nanocomposites were also anisotropic, as expected, with thermal conductivity of 201.7 $mW \cdot K^{-1} \cdot m^{-1}$ in the axial direction and 169.7 $mW \cdot K^{-1} \cdot m^{-1}$ in the radial direction. The increased thermal conductivity of AGM/PDMS can be attributed to the higher thermal conductivity of PDMS than air, as shown in Figure 4d.

Figure 4e shows that the resistance of the nanocomposite increased with the temperature, owing to the thermal expansion of PDMS. It reveals almost complete recovery when the temperature decreased. The temperature sensitivity can be

DOI: 10.1021/acsami.5b04808
ACS Appl. Mater. Interfaces 2015, 7, 19145−19152

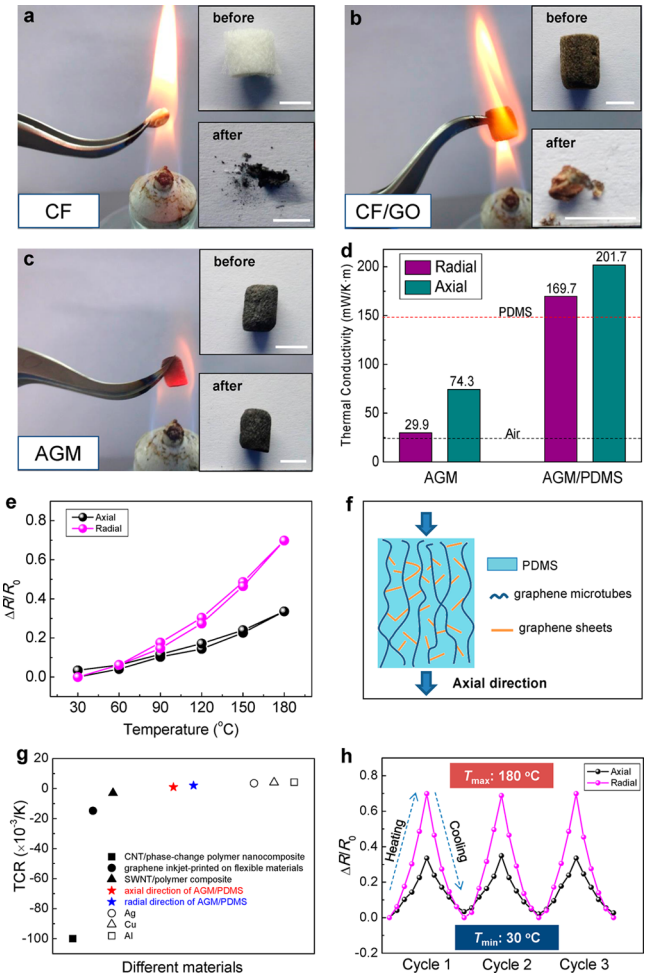

Figure 4. Flame resistance and thermal anisotropy of AGM. Photographs of (a) CF, (b) CF/GO, and (c) AGM burned with an alcohol burner. Upper insets show the pristine materials, and lower insets show the obtained materials after burning. Scale bars: 0.5 mm. (d) Thermal conductivities of AGM and AGM/PDMS. (e) Temperature-dependent resistance of AGM/PDMS. (f) Illustration of the oriented graphene microtubes in the composite, leading to the smaller TCR value in the axial direction than that in the radial direction. (g) TCR values of different materials, showing the electrical stability with temperature vibration of the composite. (h) Resistance change during heating and cooling for three cycles.

evaluated by the temperature coefficient of resistance (TCR), which is given by TCR = $R_0^{-1}(dR/dT)$, where R_0 represents the resistance at the reference temperature. It is worth noting that the TCR value in the axial direction of the composite (~0.9 × 10^{-3} K^{-1}) is lower than that in the radial direction (~2.05 × 10^{-3} K^{-1}). The phenomenon can be explained by the special structure of the composite, as illustrated in Figure 4f. PDMS filled in the slot holes along the axis (Figure S5); thus, the expansion of PDMS with temperature has a smaller influence on the axial conductivity, owing to the oriented graphene microtubes. As shown in Figure 4g, TCR values in both the axial and radial directions of the composite are smaller than those of commonly used metals, such as silver (3.5 × 10^{-3} K^{-1}), copper (4.1 × 10^{-3} K^{-1}), and aluminum (4.2 × 10^{-3} K^{-1}). Compared to previously reported composites made of carbon nanomaterials and polymers, the absolute value of TCR of AGM/PDMS is also smaller,[46−48] revealing a high electrical robustness against temperature variation. The resistance change with temperature during heating and cooling processes has been repeated three times, as shown in Figure 4h. The good repeatability as well as the low TCR value facilitated the materials as potential components in the applications of highly accurate electronic devices and circuits.

In most of the previous reports,[18,21,24] 3D porous graphene monoliths were composed of cross-linking graphene sheets with relatively poor electrical conductivity because of the random assembly. Similar to the thermal conductivity, the electrical conductivity of AGM in the axial direction was also significantly higher than that in the radial direction (as 481.2 and 112.4 S·m^{-1}, respectively), as shown in Figure 5a. The

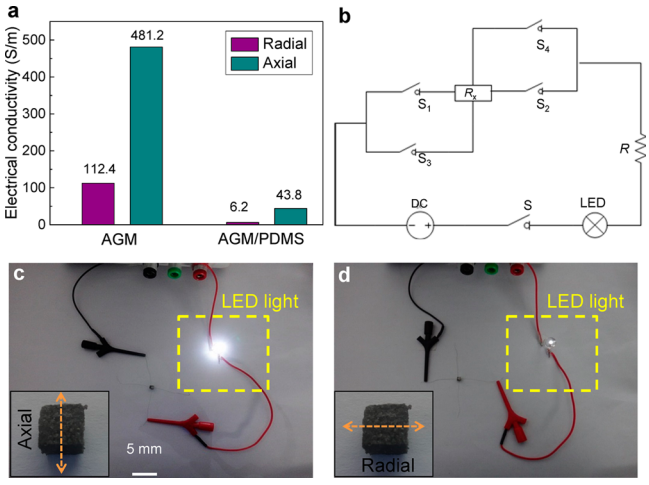

Figure 5. Electrical anisotropy of AGM. (a) Electrical conductivities of AGM and AGM/PDMS. (b) Circuit using AGM/PDMS (3 × 3 × 3 mm^3) as a resistor to light an LED. The LED is brighter (c) when AGM/PDMS is connected along the axis direction than (d) the case along the radial direction.

strong orientation-dependent feature originated from the anisotropic alignments of graphene sheets along the axis. For AGM/PDMS composite, the electrical conductivities in the axial direction of $\sigma_{//}$ and the radial direction of $\sigma_{\perp}$ were 43.8 and 6.2 S·m^{-1}, respectively. The ratio of $\sigma_{//}/\sigma_{\perp}$ was increased from 4.3 for AGM to 7.1 for AGM/PDMS. The increase of the anisotropy and the decrease of the electrical conductivity would result from the electric insulation of PDMS.

The electrical anisotropy of the AGM/PDMS can be directly observed through a circuit by the brightness of a LED light, as illustrated in Figure 5b. R_x in the circuit represents the anisotropic material. The testing material was cut into cubes to ensure that the obtained resistance in both directions can directly reflect the electrical conductivity. An electrical current through the axial direction of the material in the circuit was observed if switches S_1 and S_2 were turned on (Figure 5c). On the other hand, the electrical current would go through the radial direction when switches S_3 and S_4 were turned on (Figure 5d). In the latter case, the LED light was relatively darker (as demonstrated in the Supplementary Video 1). The results were in good agreement with the measurements of anisotropic electrical properties.

Since the electrical conductivity of the compressible polymer PDMS can be significantly increased by the continuous network of AGM, the as-prepared AGM/PDMS composites can be used as strain sensors. The relative resistance change was tested *in situ* at both axial and radial directions in the

DOI: 10.1021/acsami.5b04808
ACS Appl. Mater. Interfaces 2015, 7, 19145−19152

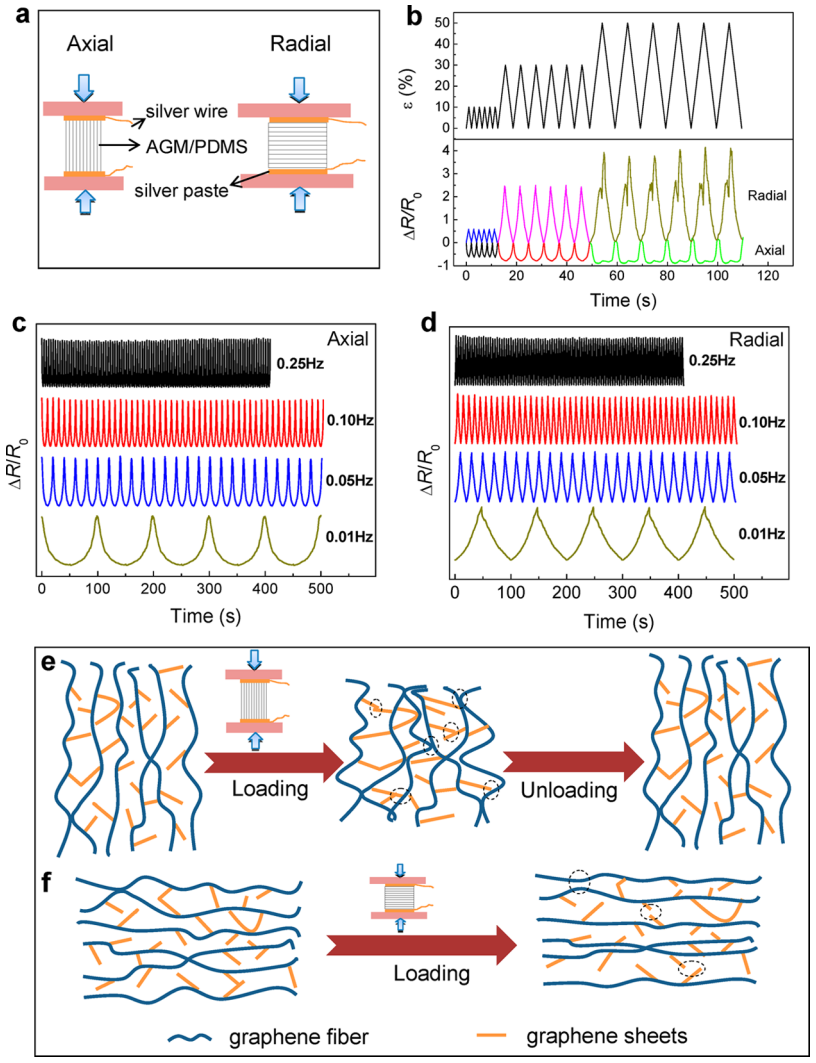

Figure 6. Electromechanical properties of AGM/PDMS. (a) Schematic illustration of *in situ* resistance measurement during compression. (b) Relative resistance changes of AGM/PDMS in radial and axial directions under different compressive strains. (c, d) Relative resistance changes under stains of different frequencies, showing no apparent frequency-dependent behavior. (e, f) Schematic illustration of the mechanism for the opposite electromechanical behavior along different directions.

compressive process, as illustrated in Figure 6a. Figure 6b shows the relative resistance change of the composite under different compressive strains. The resistance was rapidly changed in the loading stage, and it was recovered fast in the unloading stage without creep behavior. Interestingly, the resistance changed oppositely if the compressive stress was loaded in different directions. The resistance decreased with increasing loading in the axial direction and increased with increasing loading in the radial direction. The resistance change was also tested at different frequencies from 0.01 to 0.25 Hz in the axial and radial directions, as shown in Figure 6c,d. It indicated that there was no apparent frequency dependence at the applied strain of 30%.

Schematic illustrations of mechanism for the anisotropic change of electrical resistance were demonstrated in Figure 6e,f. In the mechanism, the number change of contact points in the deformation process was mainly considered. When the compression was conducted along the axis, the microtubes in the monoliths were bent and lost their stability.[44] The number of contact points increased, as shown in the black ovals in Figure 6e. The deformation was nearly completely recovered in the unloading process because of the high compressibility of PDMS. On the contrary, the number of contact points decreased in the compression vertical to the axis, because of the straightening of the microtubes that led to the separation of microtubes and the fracture of graphene sheets (Figure 6f). In Figure S6, the resistance change perpendicular to the stress direction was further measured. The number change of contact points would cause a resistance decrease in the axial loading process and a resistance increase in the radial loading process, consistent with the mechanism. The unstable change would come from the relatively unstable contact between the silver paste and AGM/PDMS in the compression process.

Figure 7 provides the direct observation of the current change in the compression process. When the composite was pressed in the axial direction, the resistance reduced, resulting in the increase of the current and the high brightness of the LED light. However, the current reduced and the light became dim when the compression was in the radial direction. Supplementary Video 2 and Supplementary Video 3 are provided, corresponding to the cases in Figure 7a,b, respectively.

DOI: 10.1021/acsami.5b04808
ACS Appl. Mater. Interfaces 2015, 7, 19145−19152

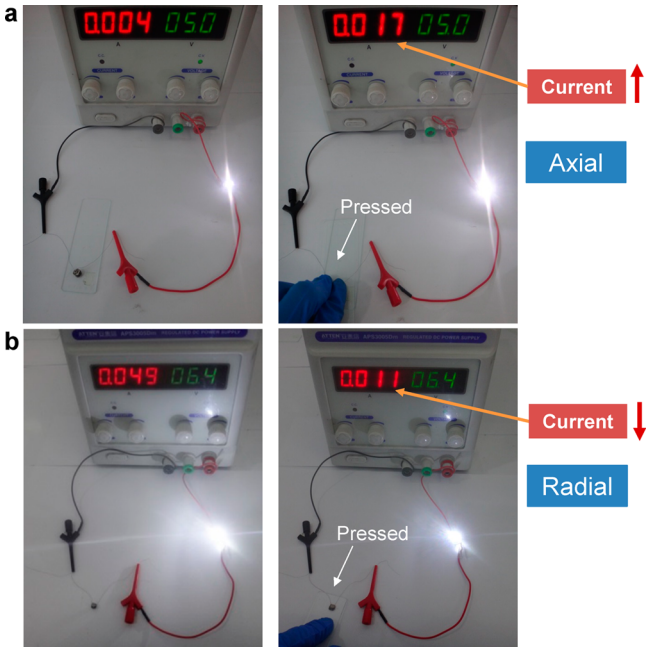

Figure 7. Direct observation of the current variation and the brightness change when AGM/PDMS was compressed in different directions. (a) Increased current and brighter LED when the compression is in the axial direction. (b) Photographs showing radial compression leads to the increase of resistance, showing decreased current and darker LED.

4. CONCLUSIONS

In summary, graphene monoliths with features of high mechanical strength, good electrical conductivity, and high thermal stability were successfully synthesized by using CFs as templates via a dip-coating method. The fabrication process is environmentally friendly for the postdisposing of toxic and nonbiodegradable CFs. The obtained novel structured materials were composed of aligned graphene microtubes connected by graphene sheets, exhibiting apparent anisotropy of mechanical, electrical, and thermal properties in the axial and radial directions. AGM/PDMS composites were further obtained by introducing compressive polymer in AGMs and the anisotropic properties were maintained. The anisotropic composites could be used in integrated circuits for current modulation based on the results of the electrical tests. The relative resistance of the composite changed oppositely under compression in the axial and radial directions. Thus, the material can detect not only the strain degrees but also the compressive directions, giving a potential application as novel electromechanical sensors. This work would provide a deeper understanding of the properties of anisotropic graphene monoliths and a substantial motivation to continue the development of this intriguing material.

■ ASSOCIATED CONTENT

Supporting Information

The Supporting Information is available free of charge on the ACS Publications website at DOI: 10.1021/acsami.5b04808.

Figures S1–S6 showing photographs of various aspects of the experiments, SEM images, XRD patterns, XPS characterizations, Raman spectra, and resistance changes and Tables S1–S3 listing comparison of previous relevant studies, mechanical characterizations of AGM/PDMS, and comparison of AGM with other reinforcements (PDF)

Video 1 (AVI)

Video 2 (AVI)

Video 3 (AVI)

■ AUTHOR INFORMATION

Corresponding Author

*E-mail: hongweizhu@tsinghua.edu.cn.

Notes

The authors declare no competing financial interest.

■ ACKNOWLEDGMENTS

This work was supported by the Beijing Science and Technology Program (Grant D141100000514001), the National Science Foundation of China (Grant 51372133), and the National Program on Key Basic Research Project (Grant 2011CB013000).

■ REFERENCES

(1) Brémaud, I.; Gril, J.; Thibaut, B. Anisotropy of Wood Vibrational Properties: Dependence on Grain Angle and Review of Literature Data. *Wood Sci. Technol.* **2011**, *45*, 735–754.

(2) Greil, P.; Lifka, T.; Kaindl, A. Biomorphic Cellular Silicon Carbide Ceramics from Wood: II. Mechanical Properties. *J. Eur. Ceram. Soc.* **1998**, *18*, 1975–1983.

(3) Glotzer, S. C.; Solomon, M. J. Anisotropy of Building Blocks and Their Assembly into Complex Structures. *Nat. Mater.* **2007**, *6*, 557–562.

(4) Akcora, P.; Liu, H.; Kumar, S. K.; Moll, J.; Li, Y.; Benicewicz, B. C.; Schadler, L. S.; Acehan, D.; Panagiotopoulos, A. Z.; Pryamitsyn, V.; Ganesan, V.; Ilavsky, J.; Thiyagarajan, P.; Colby, R. H.; Douglas, J. F. Anisotropic Self-assembly of Spherical Polymer-grafted Nanoparticles. *Nat. Mater.* **2009**, *8*, 354–359.

(5) Liu, M.; Ishida, Y.; Ebina, Y.; Sasaki, T.; Hikima, T.; Takata, M.; Aida, T. An Anisotropic Hydrogel with Electrostatic Repulsion between Cofacially Aligned Nanosheets. *Nature* **2014**, *517*, 68–72.

(6) Yao, Y.; Liu, C. H.; Fan, S. S. Anisotropic Conductance of the Multiwall Carbon Nanotube Array/Silicone Elastomer Composite Film. *Nanotechnology* **2006**, *17*, 4374–4378.

(7) Ahadian, S.; Ramon-Azcon, J.; Estili, M.; Liang, X.; Ostrovidov, S.; Shiku, H.; Ramalingam, M.; Nakajima, K.; Sakka, Y.; Bae, H.; Matsue, T.; Khademhosseini, A. Hybrid Hydrogels Containing Vertically Aligned Carbon Nanotubes with Anisotropic Electrical Conductivity for Muscle Myofiber Fabrication. *Sci. Rep.* **2014**, *4*, 4271.

(8) Gong, S.; Zhu, Z. H.; Meguid, S. A. Anisotropic Electrical Conductivity of Polymer Composites with Aligned Carbon Nanotubes. *Polymer* **2015**, *56*, 498–506.

(9) Gungor, S.; Bakis, C. E. Anisotropic Networking of Carbon Black in Glass/Epoxy Composites Using Electric Field. *J. Compos. Mater.* **2015**, *49*, 535–544.

(10) Xu, Z.; Gao, C. Graphene Chiral Liquid Crystals and Macroscopic Assembled Fibres. *Nat. Commun.* **2011**, *2*, 571.

(11) Dong, Z. L.; Jiang, C. C.; Cheng, H. H.; Zhao, Y.; Shi, G. Q.; Jiang, L.; Qu, L. T. Facile Fabrication of Light, Flexible and Multifunctional Graphene Fibers. *Adv. Mater.* **2012**, *24*, 1856–1861.

(12) Xu, Z.; Sun, H. Y.; Zhao, X. L.; Gao, C. Ultrastrong Fibers Assembled from Giant Graphene Oxide Sheets. *Adv. Mater.* **2013**, *25*, 188–193.

(13) Dikin, D. A.; Stankovich, S.; Zimney, E. J.; Piner, R. D.; Dommett, G. H. B.; Evmenenko, G.; Nguyen, S. T.; Ruoff, R. S. Preparation and Characterization of Graphene Oxide Paper. *Nature* **2007**, *448*, 457–460.

(14) Chen, H. Q.; Müller, M. B.; Gilmore, K. J.; Wallace, G. G.; Li, D. Mechanically Strong, Electrically Conductive, and Biocompatible Graphene Paper. *Adv. Mater.* **2008**, *20*, 3557–3561.

DOI: 10.1021/acsami.5b04808
ACS Appl. Mater. Interfaces 2015, 7, 19145–19152

(15) Compton, O. C.; Dikin, D. A.; Putz, K. W.; Brinson, L. C.; Nguyen, S. T. Electrically Conductive "Alkylated" Graphene Paper via Chemical Reduction of Amine-Functionalized Graphene Oxide Paper. *Adv. Mater.* **2010**, *22*, 892−896.
(16) Park, S.; Lee, K.; Bozoklu, G.; Cai, W. W.; Nguyen, S. T.; Ruoff, R. S. Graphene Oxide Papers Modified by Divalent Ions—Enhancing Mechanical Properties. *ACS Nano* **2008**, *2*, 572−578.
(17) Sumboja, A.; Foo, C. Y.; Wang, X.; Lee, P. S. Large Areal Mass, Flexible and Free-Standing Reduced Graphene Oxide/Manganese Dioxide Paper for Asymmetric Supercapacitor Device. *Adv. Mater.* **2013**, *25*, 2809−2815.
(18) Xu, Y. X.; Sheng, K. X.; Li, C.; Shi, G. Q. Self-Assembled Graphene Hydrogel via a One-Step Hydrothermal Process. *ACS Nano* **2010**, *4*, 4324−4330.
(19) Wu, Z. S.; Winter, A.; Chen, L.; Sun, Y.; Turchanin, A.; Feng, X. L.; Müllen, K. Three-Dimensional Nitrogen and Boron Co-doped Graphene for High-Performance All-Solid-State Supercapacitors. *Adv. Mater.* **2012**, *24*, 5130−5135.
(20) Niu, Z. Q.; Liu, L. L.; Zhang, L.; Shao, Q.; Zhou, W. Y.; Chen, X. D.; Xie, S. S. A Universal Strategy to Prepare Functional Porous Graphene Hybrid Architectures. *Adv. Mater.* **2014**, *26*, 3681−3687.
(21) Chen, W. F.; Yan, L. F. In Situ Self-assembly of Mild Chemical Reduction Graphene for Three-dimensional Architectures. *Nanoscale* **2011**, *3*, 3132−3137.
(22) Sheng, K. X.; Sun, Y. Q.; Li, C.; Yuan, W. J.; Shi, G. Q. Ultrahigh-Rate Supercapacitors Based on Eletrochemically Reduced Graphene Oxide for ac Line-Filtering. *Sci. Rep.* **2012**, *2*, 247.
(23) Wu, Y. P.; Yi, N. B.; Huang, L.; Zhang, T. F.; Fang, S. L.; Chang, H. C.; Li, N.; Oh, J. y.; Lee, J. A.; Kozlov, M.; Chipara, A. C.; Terrones, H.; Xiao, P. S.; Long, G. K.; Huang, Y.; Zhang, F.; Zhang, L.; Lepro, X.; Haines, C.; Lima, M. D.; Lopez, N. P.; Rajukumar, L. P.; Elias, A. L.; Feng, S. M.; Kim, S. J.; Narayanan, N. T.; Ajayan, P. U.; Terrones, M.; Aliev, A.; Chu, P. F.; Zhang, Z.; Baughman, R. H.; Chen, Y. S. Three-dimensionally Bonded Spongy Graphene Material with Super Compressive Elasticity and Near-zero Poisson's Ratio. *Nat. Commun.* **2015**, *6*, 6141.
(24) Xu, Y. X.; Wu, Q.; Sun, Y. Q.; Bai, H.; Shi, G. Q. Three-Dimensional Self-Assembly of Graphene Oxide and DNA into Multifunctional Hydrogels. *ACS Nano* **2010**, *4*, 7358−7362.
(25) Wang, Z. L.; Xu, D.; Xu, J. J.; Zhang, L. L.; Zhang, X. B. Graphene Oxide Gel-Derived, Free-Standing, Hierarchically Porous Carbon for High-Capacity and High-Rate Rechargeable Li-O2 Batteries. *Adv. Funct. Mater.* **2012**, *22*, 3699−3705.
(26) Sudeep, P. M.; Narayanan, T. N.; Ganesan, A.; Shaijumon, M. M.; Yang, H.; Ozden, S.; Patra, P. K.; Pasquali, M.; Vajtai, R.; Ganguli, S.; Roy, A. K.; Anantharaman, M. R.; Ajayan, P. M. Covalently Interconnected Three-Dimensional Graphene Oxide Solids. *ACS Nano* **2013**, *7*, 7034−7040.
(27) Chen, Z. P.; Ren, W. C.; Gao, L. B.; Liu, B. L.; Pei, S. F.; Cheng, H. M. Three-dimensional Flexible and Conductive Interconnected Graphene Networks Grown by Chemical Vapour Deposition. *Nat. Mater.* **2011**, *10*, 424−428.
(28) Yao, H. B.; Ge, J.; Wang, C. F.; Wang, X.; Hu, W.; Zheng, Z. J.; Ni, Y.; Yu, S. H. A Flexible and Highly Pressure-Sensitive Graphene-Polyurethane Sponge Based on Fractured Microstructure Design. *Adv. Mater.* **2013**, *25*, 6692−6698.
(29) Yang, Z. Y.; Jin, L. J.; Lu, G. Q.; Xiao, Q. Q.; Zhang, Y. X.; Jing, L.; Zhang, X. X.; Yan, Y. M.; Sun, K. N. Sponge-Templated Preparation of High Surface Area Graphene with Ultrahigh Capacitive Deionization Performance. *Adv. Funct. Mater.* **2014**, *24*, 3917−3925.
(30) Meng, Y. N.; Wang, K.; Zhang, Y. J.; Wei, Z. X. Hierarchical Porous Graphene/Polyaniline Composite Film with Superior Rate Performance for Flexible Supercapacitors. *Adv. Mater.* **2013**, *25*, 6985−6990.
(31) Yuan, C. Z.; Zhou, L.; Hou, L. R. Facile Fabrication of Self-supported Three-dimensional Porous Reduced Graphene Oxide Film for Electrochemical Capacitors. *Mater. Lett.* **2014**, *124*, 253−255.
(32) Zhang, R. J.; Cao, Y. C.; Li, P. X.; Zang, X. B.; Sun, P. Z.; Wang, K. L.; Zhong, M. L.; Wei, J. Q.; Wu, D. H.; Kang, F. Y.; Zhu, H. W. Three-dimensional Porous Graphene Sponges Assembled with the Combination of Surfactant and Freeze-drying. *Nano Res.* **2014**, *7*, 1477−1487.
(33) Deville, S. Freeze-Casting of Porous Ceramics: A Review of Current Achievements and Issues. *Adv. Eng. Mater.* **2008**, *10*, 155−169.
(34) Vickery, J. L.; Patil, A. J.; Mann, S. Fabrication of Graphene-Polymer Nanocomposites With Higher-Order Three-Dimensional Architectures. *Adv. Mater.* **2009**, *21*, 2180−2184.
(35) Estevez, L.; Kelarakis, A.; Gong, Q. M.; Da'as, E. H.; Giannelis, E. P. Multifunctional Graphene/Platinum/Nafion Hybrids via Ice Templating. *J. Am. Chem. Soc.* **2011**, *133*, 6122−6125.
(36) Qiu, L.; Liu, J. Z.; Chang, S. L. Y.; Wu, Y. Z.; Li, D. Biomimetic Superelastic Graphene-based Cellular Monoliths. *Nat. Commun.* **2012**, *3*, 1241.
(37) Qiu, L.; Liu, D. Y.; Wang, Y. F.; Cheng, C.; Zhou, K.; Ding, J.; Truong, V. T.; Li, D. Mechanically Robust, Electrically Conductive and Stimuli-Responsive Binary Network Hydrogels Enabled by Superelastic Graphene Aerogels. *Adv. Mater.* **2014**, *26*, 3333−3337.
(38) Lee, M.; Kim, G. P.; Song, H. D.; Park, S.; Yi, J. Preparation of Energy Storage Material Derived from a Used Cigarette Filter for a Supercapacitor Electrode. *Nanotechnology* **2014**, *25*, 345601.
(39) Polarz, S.; Smarsly, B.; Schattka, J. H. Hierachical Porous Carbon Structures from Cellulose Acetate Fibers. *Chem. Mater.* **2002**, *14*, 2940−2945.
(40) Puls, J.; Wilson, S. A.; Hölter, D. Degradation of Cellulose Acetate-Based Materials: A Review. *J. Polym. Environ.* **2011**, *19*, 152−165.
(41) Zhang, X. T.; Sui, Z. Y.; Xu, B.; Yue, S. F.; Luo, Y. J.; Zhan, W. C.; Liu, B. Mechanically Strong and Highly Conductive Graphene Aerogel and Its Use as Electrodes for Electrochemical Power Sources. *J. Mater. Chem.* **2011**, *21*, 6494−6497.
(42) Zhao, J. P.; Ren, W. C.; Cheng, H. M. Graphene Sponge for Efficient and Repeatable Adsorption and Desorption of Water Contaminations. *J. Mater. Chem.* **2012**, *22*, 20197−20202.
(43) Sun, H. Y.; Xu, Z.; Gao, C. Multifunctional, Ultra-Flyweight, Synergistically Assembled Carbon Aerogels. *Adv. Mater.* **2013**, *25*, 2554−2560.
(44) Gibson, L. J. Biomechanics of Cellular Solids. *J. Biomech.* **2005**, *38*, 377−399.
(45) Wicklein, B.; Kocjan, A.; Salazar-Alvarez, G.; Carosio, F.; Camino, G.; Antonietti, M.; Bergström, L. Thermally Insulating and Fire-retardant Lightweight Anisotropic Foams Based on Nanocellulose and Graphene Oxide. *Nat. Nanotechnol.* **2014**, *10*, 277−283.
(46) Aliev, A. E. Bolometric Detector on the Basis of Single-wall Carbon Nanotube/Polymer Composite. *Infrared Phys. Technol.* **2008**, *51*, 541−545.
(47) Kong, D.; Le, L. T.; Li, Y.; Zunino, J. L.; Lee, W. Temperature-Dependent Electrical Properties of Graphene Inkjet-Printed on Flexible Materials. *Langmuir* **2012**, *28*, 13467−13472.
(48) Fernandes, G. E.; Kim, J. H.; Sood, A. K.; Xu, J. Giant Temperature Coefficient of Resistance in Carbon Nanotube/Phase-Change Polymer Nanocomposites. *Adv. Funct. Mater.* **2013**, *23*, 4678−4683.

DOI: 10.1021/acsami.5b04808
ACS Appl. Mater. Interfaces 2015, 7, 19145−19152